

MIT Open Access Articles

Granular Thermodynamics

The MIT Faculty has made this article openly available. **Please share** how this access benefits you. Your story matters.

Citation: Shattuck, M. D., R. A. Ingale, and P. M. Reis. "Granular Thermodynamics." Ed. Masami Nakagawa & Stefan Luding. AIP Conference Proceedings 1145.1 (2009): 43-50. ©2009 American Institute of Physics

As Published: <http://dx.doi.org/10.1063/1.3179956>

Publisher: American Institute of Physics

Persistent URL: <http://hdl.handle.net/1721.1/60233>

Version: Final published version: final published article, as it appeared in a journal, conference proceedings, or other formally published context

Terms of Use: Article is made available in accordance with the publisher's policy and may be subject to US copyright law. Please refer to the publisher's site for terms of use.



Granular Thermodynamics

M. D. Shattuck*, R. A. Ingale* and P. M. Reis†

**Benjamin Levich Institute, The City College of the City University of New York, 140th Street and Convent Avenue, New York, New York 10031, USA*

†*Department of Mathematics, Massachusetts Institute of Technology, Cambridge 02139, USA*

Abstract. We present experimental evidence for a strong analogy between quasi-2D uniform non-equilibrium steady states (NESS) of excited granular materials and equilibrium thermodynamics. Under isochoric conditions we find that the structure of granular NESS, as measured by the radial distribution function, the bond order parameter, and the distribution of Voronoi cells, is the same as that found in equilibrium simulations of hard disks. Three distinct states are found corresponding to a gas, a dense gas, and a crystal. The dynamics of the dense gas is characterized by sub-diffusive behavior on intermediate time scales (caging). Under isobaric conditions we find a sharp first-order phase transition characterized by a discontinuous change in density and granular temperature as a function of excitation strength. The transition shows rate dependent hysteresis but is completely reversible if the excitation strength changes quasi-statically. All of these behaviors are analogous to equilibrium thermodynamics. The one difference is the velocity distributions, which are well described by $P(c) = f_{MB}[1 + a_2 S_2(c^2)]$, in the range $-2 < c < 2$, where $c = v/\sqrt{2T}$, v is one component of the velocity, T is the granular temperature, f_{mb} is a Maxwell-Boltzmann and S_2 is a second order Sonine polynomial. The single adjustable parameter, a_2 , is a function of the filling fraction, but not T . For $|c| \geq 2$, $P(c) \propto \exp(-A \times c^{-3/2})$ as observed in many other experiments.

Keywords: Granular Materials, Non-equilibrium Steady-State

PACS: 47.57.Gc, 05.70.Ln, 81.05.Rm, 01.50.Pa

INTRODUCTION

According to thermodynamics, the equilibrium state of a system is completely determined by a small number of state variables, for example, the temperature, the pressure, and density. The equilibrium state, which relies on the fact that particle interactions conserve energy, is homogeneous and steady (time-independent). However, in a granular system (collection of macroscopic particles) interactions do not conserve energy. Therefore, the true equilibrium state of the system is one in which all particles are at rest. However, a steady flow of energy into a granular ensemble can produce a steady-state in which the energy input balances the energy loss through collisions [1, 2, 3]. We refer to this as a non-equilibrium steady state (NESS) to emphasize the fact that, although it is time-independent (steady), it is not in equilibrium due to energy flow through the system. Under the appropriate conditions a NESS can also be homogeneous. Here we use laboratory experiments to explore the extent to which a homogeneous NESS is an analog to the equilibrium state of thermodynamics. By analogy with ordinary fluids flows, which are assumed to be locally in thermodynamic equilibrium, this will pave the way for analysis of inhomogeneous time-dependent granular flow by assuming local (in time and space) uniform NESS.

We explicitly test the microscopic structure[1], diffusion[2], and velocity distributions[3] to see how they differ from equilibrium. We examine the phase be-

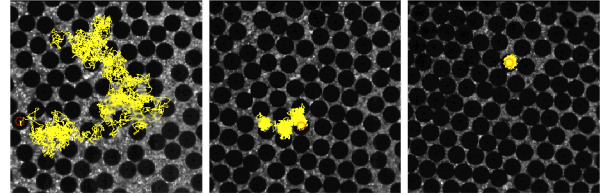


FIGURE 1. Experimental frames with superposed typical trajectories of a single particle: (Left) $\phi = 0.567$, (Center) $\phi = 0.701$ and (Right) $\phi = 0.749$. Note that even though only a single trajectory is shown for each ϕ , particle tracking and statistics were collected for all particles in the imaging window. The particle diameter is 1.19mm.

havior of the system under constant volume conditions (isochoric) using the bond order parameter. We look for phase transitions under constant pressure (isobaric). To be useful, a granular NESS must be entirely determined by a small number of state variables just as in ordinary thermodynamics. This requirement means that phase transitions must be reversible with no hysteresis under quasi-static parameter changes.

Structure, Diffusion, and Phase: We find [1] that the structure of the uniform granular NESS is identical to the equilibrium state found in Monte Carlo simulations of elastic hard disks from the literature [4]. We find that the state of the system under isochoric conditions is solely determined by the density or filling fraction ϕ with three phases: gas, intermediate, and crystal (Fig. 1). The phase

boundaries, ϕ_l (*liquidus point*) and ϕ_s (*solidus point*) are determined by structure alone [1]. In the gas phase the system is characterized by diffusive behavior. The intermediate phase is the same as that of equilibrium hard sphere/disk systems [5, 6, 7] showing the distinct signature of caging behavior (i.e., subdiffusive behavior at intermediate times, see Fig. 6, followed by diffusive behavior at long times) and is consistent with the hexatic phase in 2D equilibrium hard disks [8]. In the crystalline phase particles do not diffuse and sit in a system-filling hexagonal lattice for all times studied. Under isobaric conditions, we find a discontinuous, first-order phase transition from a disordered gas to an ordered crystal. The state of the system is determined by the strength of the energy input Q , the number of particles N , and the pressure P . Q is analogous to temperature in thermodynamics. The granular temperature T (kinetic energy per particle), and volume V are then determined by Q , N , and P . The transition shows rate-dependent hysteresis as a function of dQ/dt , which becomes reversible as the rate slows ($dQ/dt \rightarrow 0$).

Velocity Distribution: The velocity distributions, however, differ slightly from that of equilibrium systems. They are well described by $P(c) = f_{MB}[1 + a_2 S_2(c^2)]$, in the range $|c| < c^*$, where $c = v/\sqrt{2T}$, $c^* = 2$, v is one component of the velocity, T is the granular temperature, f_{mb} is a Maxwell-Boltzmann, and S_2 is a second order Sonine polynomial. The single adjustable parameter, a_2 , is a function of the filling fraction, but not T . For $|c| \geq c^*$, $P(c) \propto \exp(-A \times c^{-3/2})$ as observed in many other experiments [9, 10]. In equilibrium systems, $a_2 = 0$ and $c^* \rightarrow \infty$.

In order to test the applicability of equilibrium thermodynamic ideas to granular NESS, we have developed two experimental systems to generate quasi-two dimensional granular fluids in NESS. In the first, we inject energy in a spatially homogeneous way at constant volume (isochoric) to produce a horizontal 2D *uniformly heated* granular layer [1, 2, 3]. In the second, energy is injected through the bottom boundary into a vertical 2D cell under constant pressure (isobaric).

Horizontal Isochoric Cell: In the isochoric cell the main experimental parameter is the filling fraction, $\phi = N[d/(2R)]^2$, where N is the total number of spheres, with diameter d in a cell of radius $R = 50.8\text{mm}$. ϕ is systematically varied from a single particle to hexagonal close packing. Our experimental apparatus is adapted from a geometry originally introduced by Olafsen and Urbach [9]. We inject energy into a collection of $d=1.191\text{mm}$ stainless steel spheres by sinusoidal vertical vibration using an electromagnetic shaker at a frequency f and dimensionless maximum acceleration, $\Gamma = A(2\pi f^2/g)$, where A is the amplitude of vibration and g is the gravitational acceleration. We typically work within the experimental ranges ($10 < f < 100\text{Hz}$ and $1 < \Gamma < 6$). We

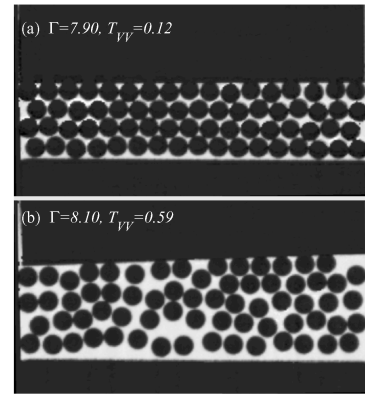


FIGURE 2. Photographs of a 2D granular layer, with freely floating (isobaric) weight: (a) $\Gamma = 7.90$, $T_{VV} = 0.12$, crystal. (b) $\Gamma = 8.10$, $T_{VV} = 0.59$, gas.

confine the spheres to a fixed cylindrical volume (cylindrical axis parallel to gravity) using a horizontal stainless steel annulus (85.3d inner diameter) and sandwiched between two glass plates. The thickness of the annulus sets the height of the cell which can be varied from $1.05d$ to 2.5 . The top glass plate is optically flat, but the bottom plate is roughened by sand-blasting generating random structures from $50\mu\text{m}$ to $500\mu\text{m}$. The roughened bottom surface increases the energy injected into the horizontal velocities over a flat surface, as discussed in detail in [3]. It is this innovation, which allows us to study a wider range of filling fractions ($1.4 \times 10^{-4} < \phi < 0.8$) than in previous work. We record the dynamics of the system using high speed photography at 840Hz and track the particle trajectories in a $(15 \times 15)\text{mm}^2$ central region to avoid boundary effects (see Fig. 1).

We have developed high-precision particle tracking software using two-dimensional least squares minimization of the particle positions, which is able to find 100% of the N particles in the imaging window and resolve the position $\vec{x}_n(t)$ of a particle n to sub-pixel accuracy at each time step. In our imaging window we were able to achieve resolutions of $1/50$ of a pixel (which corresponds to $1\mu\text{m}$). Our algorithm constructs trajectories of the particles allowing the calculation of the particle velocities $\vec{v}_n(t)$, and other derived quantities.

From these data we measure the filling fraction ϕ , granular temperature $T = 1/(2N) \sum_{n=1}^N \vec{v}_n^2(t)$, velocity distributions $P(\vec{v})$, and Voronoi constructions.

Vertical Isobaric Cell: In the isobaric system, there are three control parameters, the energy injection strength Q , the pressure P , and the number of particles N . We place N (34–85) monodisperse stainless steel spherical ball bearings of diameter $D = 3.175\text{mm}$ in a container $L = 17.5D$ wide by $H = 20D$ tall by $1D$ deep, as shown in Fig. 2. A thin plunger slides

through a slot at the bottom of the cell and oscillates sinusoidally to excite (heat) the particles from below. As a proxy for Q , the driving is characterized by Γ and f just as in the horizontal isochoric system. The key difference in this experiment is a freely floating weight that confines the particles from the top, allowing the volume to fluctuate but providing constant pressure conditions $P = Mg/L = W/L$, where W is the weight and M is the mass of the floating weight. The weight not only provides a constant (time-independent) pressure, it also aids in creating a more uniform pressure over the height of the cell. Due to gravity the pressure drop ΔP across the granular layer is the weight of the layer W_l (i.e., $\Delta P = (P + W_l/L) - P = W_l/L = Nmg/L$, where m is the particle mass). The average pressure is $\bar{P} = (P + W_l/L)/2 = (W + W_l)/2L$, and the relative pressure variation is $\delta P = \Delta P/\bar{P} = 2W_l/(W + W_l)$. Thus, $0 < \delta P < 2$, with the maximum at $W = 0$ or no floating weight. We find that for $W < W_l/2$, $\delta P > 4/3$ the inhomogeneity of the pressure leads to other effects, such as surface fluidization as previously seen in similar systems (e.g., [11]). In the current studies W is always greater than W_l or $\delta P < 1$.

We use the same high-speed digital photography system developed for the isochoric system to measure the positions of the plunger, the weight, and all of the particles in the cell with a relative accuracy of 0.04% of D or approximately $1.2\mu\text{m}$ at a rate of 840 Hz. We track the particles from frame to frame and assign a velocity to each one, typically $\sim D/5$ per frame.

From these data we measure the cell volume, average density and granular temperature (i.e., average kinetic energy per particle). In our study, we focus on the behavior of the system for an integer number of rows, which is initially in a perfect crystalline state. To prepare the system initially in the densest state, we increase Γ to 16 and then slowly lower the acceleration to zero. From this state we increase Γ in 256 steps until $\Gamma = 16$ and then decrease in another 256 steps until $\Gamma = 0$. At each step we take data. The time for each step is variable but typically 1–10s.

RESULTS

We compare the 2D uniformly-heated horizontal isochoric granular NESS described above to equilibrium systems. We focus on three important aspects: structure, diffusion (caging dynamics), and velocity distributions. In this system, three phases emerge depending on the filling fraction ϕ as shown in Fig. 1—gas, intermediate, and crystal. The boundaries of these phases are determined by the orientational structure of the particle as described below.

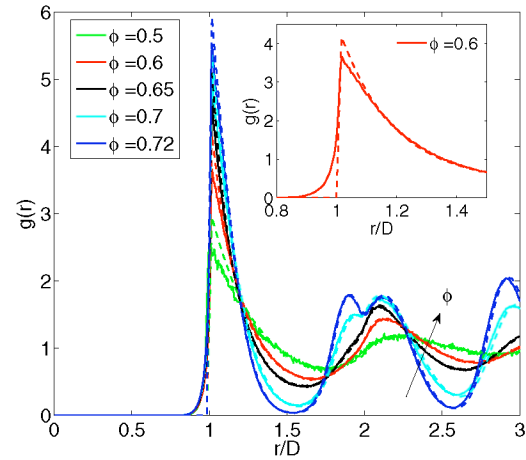


FIGURE 3. Experimental (solid) and numerical (dashed, extracted from [4]) curves of the radial distribution functions for 5 values of ϕ . The arrow points in the direction of decreasing ϕ . Inset: Section of $g(r)$ curve for $\phi = 0.6$.

Structure: We identify three key microscopic measures to compare the structure of the isochoric granular NESS to equilibrium system: radial distribution function, bond order parameter, and shape factor [4]. Each one focuses on a different aspect of the structure—the radial distribution on positional order, the bond order parameter on orientational order, and the shape factor on the topology of Voronoi cells. For comparison we used recent Monte-Carlo simulation of hard disks by Moucka and Nezbeda [4]. The validity of Monte-Carlo simulation depends on equilibrium assumptions so this provide a valuable comparison. For more details on these and other measures in our granular NESS see [1].

Radial Distribution Function: The radial distribution function $g(r)$ is a standard way of describing the average positional structure of particulate systems [12]. $g(r)$ measures the probability that two particle centers are a distance r apart regardless of orientation. For hard particles there is zero probability that the particles overlap so $g(r) = 0$ for $r < d$, where d is the diameter of the particles.

In Fig. 3 we plot $g(r)$ for several ϕ . For low filling fractions ($\phi < 0.65$) we observe fluid-like behavior, and $g(r)$ has peaks at $r/d \simeq 1, 2$ and 3 , as is commonly seen in hard sphere simulations [12]. The peaks represent correlations in the distances between particles. At higher densities ($0.65 < \phi < 0.72$), $g(r)$ develops a shoulder below the $r/d = 2$ peak, which evolves into a distinct peak located at $r/d = \sqrt{3}$, signifying strong hexagonal packing. For each $g(r)$ experimental curve in Fig. 3, we have superposed a corresponding (dashed) curve from the Monte Carlo simulation of equilibrium hard disks of Moucka

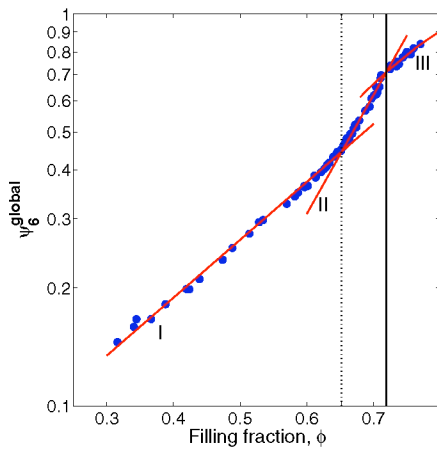


FIGURE 4. Semi-logarithmic plot of the bond-orientational order parameter, ψ_6 . The first two lines, I and II, are least squares fits of the form $\psi \sim \exp[A\phi]$ and line III is a linear fit of the form $\psi \sim A\phi$. The dashed and solid vertical lines are located at $\phi_l = 0.652$ and $\phi_s = 0.719$, respectively.

and Nezbeda [4], for identical values of ϕ . The agreement for $r/d > 1.1$ is so good that most of the numerical curves are hidden by the experimental curves. There are no fitting parameters; the curves only depend on ϕ , which is measured directly in the experiments and the simulations. The only discrepancies occur for $r/d < 1.1$, as shown in the inset of Fig. 3 for $\phi = 0.60$. This deviation is due to the fact that in granular NESS the system is not composed of 2D disks, but 3D spheres in a thin geometry. This leads to out-of-plane collisions and an apparent particle overlap, since we measure only the 2D projection. This also lowers the *measured* value of $g(r)$ at contact $g(d)$, which is important in kinetic theories, but the *actual* value, which can be estimated from the known layer thickness of $1.6d$, is consistent with the equilibrium value. From these measurements the structure of granular NESS is essentially indistinguishable from the equilibrium structure.

Bond Order Parameter: The global bond-orientational order parameter ψ_6^{global} measures the extent to which particles have 6-fold (hexagonal) orientational order regardless of distance. In equilibrium systems angular correlations also arise as ϕ is increased [13]. These correlations are quantified by $\psi_6^{\text{global}} = |1/N \sum_{i=1}^N 1/M_i \sum_{j=1}^{M_i} e^{i6\theta_{ij}}|$, where N is the number of particles in the observation window, θ_{ij} is the angle between the particles i and j and a fixed reference, and M_i is the number of nearest neighbors of particle i , found using the Voronoi construction [14]. ψ_6^{global} is 0 for random positions and 1 for perfect hexagonal order.

In Fig. 4 we plot the dependence of ψ_6^{global} on ϕ . The

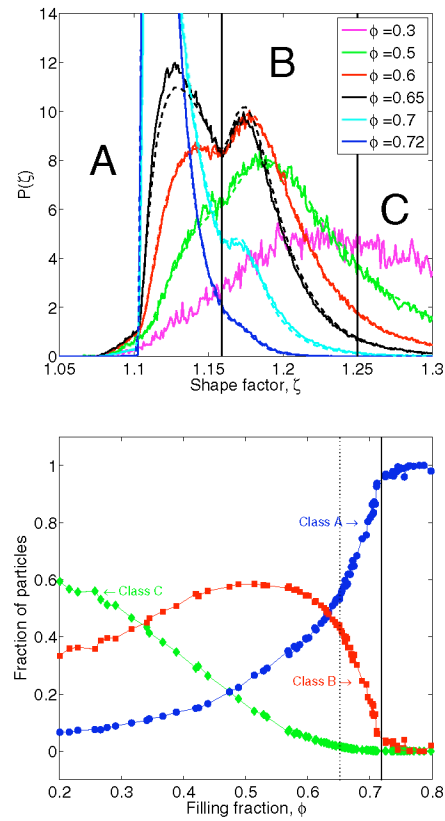


FIGURE 5. (Top) Plot for the probability distribution functions of shape factor, $P(\zeta, \phi)$ for 6 values of ϕ . The two vertical lines located at $\zeta = 1.159$ and $\zeta = 1.25$ divide the Voronoi cell types into 3 classes, A, B and C. Experimental curves are solid and numerical are dashed (extracted from [4]). (Bottom) Fraction of particles in each of the 3 classes A, B and C, (defined in Top panel) as a function of filling fraction.

value of the bond orientational order parameter tends to unity in the crystal phase, but $\psi_6^{\text{global}} \ll 1$ for a disordered phase. Two different *phase boundaries*: $\phi_l = 0.652$ and $\phi_s = 0.719$ can be identified in Fig. 4 based on the slope of $\psi_6(\phi)$. The experimental behavior is identical to equilibrium behavior, in which a two-step continuous phase transition is observed during 2D crystallization [13]. First, the isotropic fluid phase develops long range angular order creating a hexatic phase, then the hexatic phase develops long range positional order creating a crystalline phase.

Shape Factor: To examine the structure in more detail we examine the local topology of Voronoi cells using the shape factor ζ as defined by Moucka and Nezbeda [4]. The shape factor is a sensitive measure used to quantify structural changes in the fluid-to-crystal transition in 2D. ζ is defined at the particle level, using Voronoi tessellation, as $\zeta_i = C_i^2/4\pi S_i$, where S_i is the surface area

and C_i the perimeter of the Voronoi cell of the i^{th} particle. For circles $\zeta = 1$ and $\zeta > 1$ for all other shapes ($\zeta = 4/\pi \sim 1.273$ for square, $\zeta = \pi/5 \tan(\pi/5) \sim 1.156$ for regular pentagons, and $\zeta = 6/\sqrt{3}\pi^2 \sim 1.103$ for regular hexagons). Therefore, ζ quantifies the topology of the Voronoi cells associated with the individual particles.

In Fig. 5(top) we present a plot of the distribution of shape factors, $P(\zeta, \phi)$ for several ϕ . We superpose numerical data (dashed lines) from Monte Carlo simulations of equilibrium hard disks [4], for the same values of ϕ , and find that our experimental results are nearly identical with the numerical simulations with no adjustable parameters. For low ϕ , $P(\zeta)$ is broad with a flat maximum, representing a random distribution of Voronoi cell types. As ϕ is increased, $P(\zeta)$ becomes localized around a maximum, which moves toward lower values of ζ . Eventually, for $\phi > 0.5$ a distinct second maximum appears. At the crystallization point, $\phi_s = 0.719$, the original maximum disappears and the new maximum centered at $\zeta \approx 1.1$, the value for regular hexagons, rises sharply. The two maxima suggest at least two distinct classes of shapes.

To quantify the classes (A, B, and C) we follow the classification scheme proposed by Moucka and Nezbeda, as shown in Fig. 5(top). The boundary between classes A and B is set at the non-zero minimum of $P(\zeta)$ which is only weakly dependent on ϕ and has an average value of $\zeta_{min} = 1.159$. The upper ζ cut-off $\zeta_u = 1.25$ for class B is set so that when the two maxima of $P(\zeta)$ are equal, the number of particles in classes A and B types are equal (i.e., $\int_0^{\zeta_{min}} P(\zeta) d\zeta = \int_{\zeta_{min}}^{\zeta_u} P(\zeta) d\zeta$).

In Fig. 5(bottom) we plot the fraction of particles of each type $n_A(\phi)$, $n_B(\phi)$, $n_C(\phi)$ as a function of ϕ . The plot shows a clear change in the slope of $n_A(\phi)$ and $n_B(\phi)$ at $\phi_s = 0.719$, the onset of crystallization. There are several features near ϕ_l . For example, $n_A(\phi) \simeq n_B(\phi)$ and $n_C(\phi) \simeq 0$. However, these features are not sharp and would yield a different value of ϕ_l . Further, it is not clear why having equal numbers of type A and B is significant. Regardless of the meaning of these features, they are exactly the same for granular NESS and equilibrium hard disk simulations.

Caging dynamics: Fig. 1 shows typical single particle trajectories in each of the three phases found in granular NESS. Simple fluid behavior is observed at low ϕ , characterized by random diffusion (Fig. 1(left)). Above crystallization ($\phi > \phi_s$) the particles are completely confined by their six hexagonally packed neighbors (Fig. 1(right)). In the intermediate phase, both behaviors are seen but on different time scales (Fig. 1(center)). At short times, particles are trapped in cages formed by their neighbors, but they eventually escape to another cage and at long times they diffuse from cage to cage. We use the Mean Square Displacement (MSD) to show that the caging dynam-

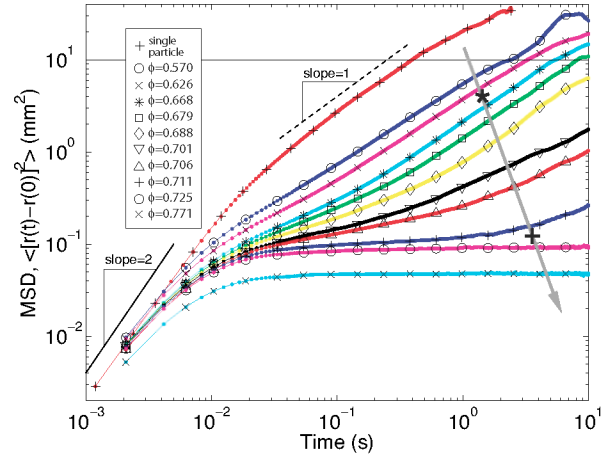


FIGURE 6. Time dependence of the Mean Square Displacement for various values of filling fraction (numerical values shown in the box), except for the upper most curve (+) which is for a single particle in the cell. The arrow points in the direction of increasing ϕ . Along the arrow, the symbols (*) and (+) are located at ϕ_l and ϕ_s , respectively, to help place the curves in the fluid's phase diagram. The horizontal line (located at 9.954 mm²) corresponds to the square of 1/4th of the linear dimension of the imaging window, above which finite system size effects become important.

ics seen here is qualitatively identical to that of ordinary dense fluid systems like colloids [5, 15] and supercooled liquids [16].

We examine the MSD of the particle to more fully understand the dynamic state of the system and to further compare granular NESS with equilibrium systems. The MSD $M(t) = \langle [\vec{x}(t) - \vec{x}(0)]^2 \rangle$, where $\vec{x}(t)$ is the position of a particle at time t , $\vec{x}(0)$ is its initial position, and the brackets $\langle \cdot \rangle$ represent ensemble averaging over many realizations. A log-log plot of $M(t)$ for a range of ϕ is shown in Fig. 6. Generally, $M(t) \sim t^{\alpha(t)}$, and α is used to characterize the motion. At the shortest times the motion of the particles is ballistic, $\alpha = 2$. They simply move according to $\vec{x}(t) = vt$, and $M(t) \sim t^2$, which gives a slope of 2 on the log-log plot. At the lowest density (marked with a +) there is only a single particle in the cell, which moves diffusively and the slope of $M(t)$ tends to 1. This shows that the trajectory of a single particle is randomized over the cell.

Three types of behavior are seen in our granular NESS, corresponding to the three snapshots in Fig. 1. At low densities ($\phi < 0.6$, Fig. 1(left)), the particle motion is diffusive. This means that $\alpha \geq 1$ with $\alpha = 1$ at long times. For high densities ($\phi > 0.719$, Fig. 1(left)) the particles are trapped in their crystalline cells, and $M(t)$ becomes a constant value set by the lattice spacing with $\alpha = 0$. However, in the intermediate phase ($0.6 < \phi < 0.719$, Fig. 1(center)) a plateau develops at in-

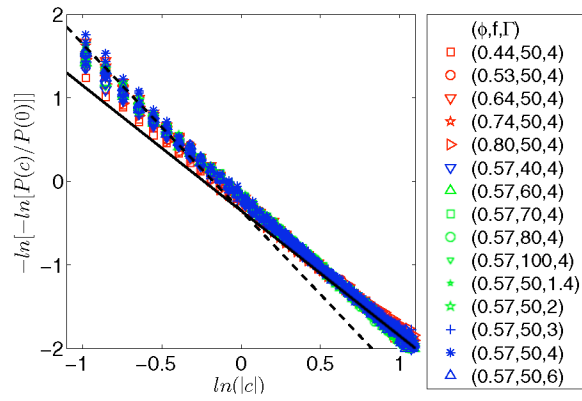


FIGURE 7. Double log plot of the tails of $P(c)$ for many filling fractions (ϕ), frequencies (f) and acceleration (Γ). The solid line correspond to stretched exponentials of the form $\sim \exp(-A|c|^{3/2})$ whereas the dashed lines correspond to the Gaussian behavior of the form $\sim \exp(-Ac^2)$.

intermediate times where the motion is sub-diffusive with $0 < \alpha < 1$. This plateau appears just before the liquidus point $\phi_l = 0.652$ and gradually becomes increasingly visible above ϕ_l (marked as * in Fig. 6 to orient the curves in the phase diagram). This represents the slowing down due to the cage effect as shown in Fig. 1(center).

This behavior is the same as that seen in equilibrium systems. We have also compared a number of other measures in [2], which show similar agreement with equilibrium systems. In molecular systems this behavior is typically observed indirectly from scattering experiments [15]. In colloids, however, caging motion has been observed directly through microscopy, in both 3D [5] and quasi-2D [6] geometries. A large number of theoretical [17, 18] and numerical [7, 19] studies have set out to further investigate the importance of this heterogeneous dynamics. The relevance of caging in driven granular materials [20, 21] and air-fluidized particle systems [22] has only recently started to be addressed.

Velocity distributions: As described above the isochoric granular NESS is nearly identical to its equilibrium counterpart in structure and diffusion. However, there are a few differences. The most important is in the single particle velocity distribution $P(\vec{v})$. This distribution is a Maxwell-Boltzmann for equilibrium fluids. $f_{MB}(\vec{v}) = A \exp[-\vec{v}^2/(2T)]$, where the mass of the particles is set to 1 and T is the equilibrium temperature measured in units of energy (i.e., T is the average kinetic energy per particle). To look for deviation from this in granular NESS, we focus on the distribution of a scaled single component of the velocity $c = v/\sqrt{(2T)}$, where v is the unscaled velocity component and T , the granular temperature or average kinetic energy of the particles. In defining T we set the mass to 1 for convenience, so

that T is also, the variance of $P(v)$. Then, the normalized Maxwell-Boltzmann is $f_{MB}(c) = 1/\sqrt{\pi} \exp(-c^2)$.

Deviations from the Maxwell-Boltzmann distribution in granular material are well established [9, 10]. In particular, we distinguish between deviations at low velocities ($|c| < 2$) and at high velocities or tails ($|c| \geq 2$). Previous experiments focused on the tails, which represent less than 0.5% of the velocities. It is seen that experimental distributions exhibit a considerable overpopulation and have been shown to scale as $\exp[-A|c|^\gamma]$, $\gamma = 3/2$. This behavior is in agreement with numerical [23] and theoretical [24] predictions. We see the same behavior as shown in Fig. 7 for many experimental conditions. The double logarithm creates a curve with slope equal to γ . Even though these tails correspond to events with extremely low probabilities, they increase the variance of the distribution and T and leads to a major discrepancy in the region of high probability in the low velocity portion of the distribution [25] which have, thus far, been greatly overlooked in experimental work.

The velocity distribution is of fundamental importance in kinetic theories of granular material (see e.g., [26]). As a result, there have been many theoretical and numerical studies on velocity distribution in granular NESS [23, 27] in which the steady state velocity distribution has been found to deviate from the Maxwell-Boltzmann distribution. van Noije and Ernst [24] studied these velocity distributions using approximate solutions to the inelastic hard sphere Enskog-Boltzmann equation by an expansion in Sonine polynomials. Their theoretical analysis has been validated by numerical studies in both molecular dynamics [23] and direct simulation Monte Carlo [28, 29]. The use of Sonine corrections is particularly attractive since it leaves the variance of the resulting velocity distribution unchanged but leads to a non-Gaussian fourth moment or kurtosis, $K \neq 3$.

For low velocities ($|c| < 2$), which corresponds to high probability ($> 99.5\%$) the experimental velocity distribution in granular NESS fits $P(c) = f_{MB}(1 + a_2 S_2(c^2))$ where $S_2(x) = (1/2x^2 - 3/2x + 3/8)$ is the 1D second order Sonine polynomial. a_2 , the only new fitting parameter, is a function of filling fraction ϕ alone [3]. In Fig. 8 we plot $\Delta(c) = P(c)/f_{MB}(c) - 1$. The result is a function, which is well represented by $S_2(c^2)$. Also shown in Fig. 8 is a fit to higher order Sonine corrections. While these higher order corrections improve the fit slightly, it does not justify adding new parameters [3].

The phase transition to crystalline order in the isochoric NESS and in analogous equilibrium systems is second order and proceeds through the complicated hexatic [13] or intermediate phase. To see if a first-order phase transition exists in a granular NESS, we examine the isobaric (constant pressure) system described above. For the results described below, we fix the number $N = 68$, the pressure P , and varied the energy injection

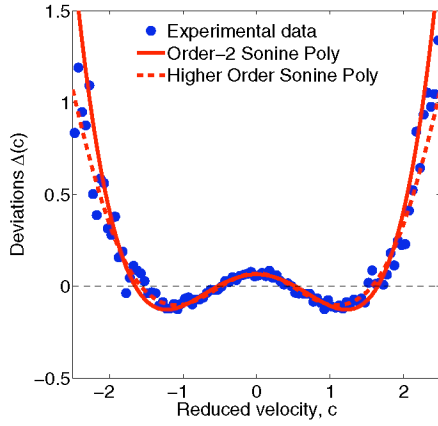


FIGURE 8. Experimental deviation function from Gaussian behavior, $\Delta(c)$ for $\phi = 0.66$. The solid line is the Sonine polynomial $a_2(1/2c^4 - 3/2c^2 + 3/8)$ with one single fitting parameter: $a_2 = 0.171$. The dashed line is the higher order Sonine polynomial description of the form $\sum_{p=2}^6 a_p S_p(c^2)$ with the following (five fitting parameters) Sonine coefficients; $a_2 = 0.1578$, $a_3 = -0.0656$, $a_4 = 0.1934$, $a_5 = -0.1637$ and $a_6 = 0.0832$.

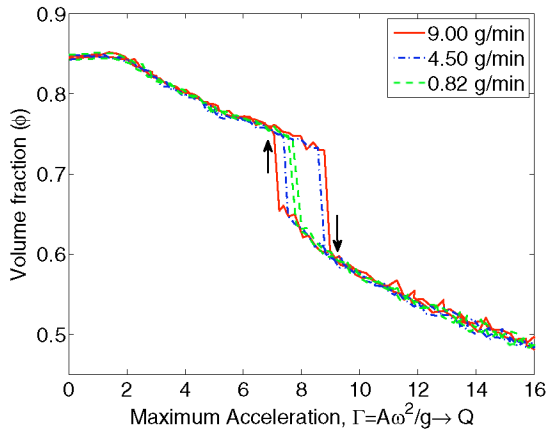


FIGURE 9. Plot of the filling fraction (ϕ) as a function of increasing and decreasing Γ (as indicated by the arrows) at 50 Hz, under isobaric conditions. The volume fraction plots are shown for three different heating rates ($d\Gamma/dt$); 9.00g/min (solid line), 4.50g/min second (dotted-dashed line) and 0.82g/min (dashed line) to illustrate the hysteretic behavior of the phase transition. g is the gravitational constant.

strength Q . We measure the filling fraction ϕ and granular temperature T . As a proxy for Q , we use Γ , the maximum acceleration measured in units of the gravitational constant $g = 9.8m/s^2$ at fixed frequency $f = 50Hz$. A better proxy for Q is $\Gamma/(2\pi f)$, which is $\propto \Gamma$ at constant f .

First-order phase transition: Depending on the value of $Q = \Gamma$ two states can exist, as shown in Fig.

2. For $\Gamma < 8$ the system is in a crystalline state as shown in Fig. 2(top). For $\Gamma > 8$ the system is in a gas state as shown in Fig. 2(bottom). Even though the value of Γ differs by only 2.5%, across the transition the filling fraction ϕ changes from $\phi_s = 0.743 \pm 0.005$ to $\phi_l = 0.632 \pm 0.006$ or 16% and the granular temperature, T_{VV} changes from $0.12 \pm 0.04(m/s)^2$ to $0.59 \pm 0.08(m/s)^2$ or a factor of 5. The errors in ϕ and T represent the run to run deviations. The temperature, T_V , is the vertical velocity variance, which is different from the horizontal velocity variance. Anisotropic granular temperature is common in granular NESS when the forcing is only applied in one direction.

To check the reversibility of this transition we measure ϕ and T as a function of Γ . The results for ϕ are shown in Fig. 9. The T dependence is similar, but not shown for clarity. The plot shows $\phi(\Gamma)$ as Γ is increased and decreased as indicated by the arrows. Following the solid curve starting from $\Gamma = 0$, the system is in the densest crystalline state. As Γ is increased the crystal begins to expand and ϕ decreases. At $\Gamma \simeq 9$ there is a sharp change in the density as the system goes from a crystalline state to a gaseous state. The sharp change is the hallmark of a first-order phase transition. As Γ is increased further the gas expands and ϕ decreases smoothly. When Γ is decreased starting from 16 the system traces the same (reversible) path until $\Gamma < 9$ where hysteresis is clearly visible. At $\Gamma \simeq 7$ the system freezes by a discontinuous change in the density to a crystalline structure and then follows a reversible path back to $\Gamma = 0$.

This is analogous to an equilibrium first-order sublimation phase transition (e.g. melting/freezing dry ice), in which Γ plays the role of temperature. The hysteresis represents super-cooling and super-heating. Moreover, just as in an equilibrium phase transition the hysteresis can be eliminated, by slowing down the rate of change of the control parameter. In this case, decreasing the rate of change of Γ by a factor of 2 reduces the hysteresis as shown by the dot-dash curve. By decreasing by another factor of 5 a completely reversible, discontinuous transition is produced curve is produced as shown by the dashed curve.

CONCLUSION

We have shown that uniform granular NESS behave very much like their equilibrium counterparts. This is surprising since energy is not conserved and must be supplied to the system. The isochoric granular NESS has nearly identical structure as compared to equilibrium simulations of hard disks. The particle diffusion shows caging behavior just like that of equilibrium systems. The velocity distribution differs slightly from the equilibrium Maxwell-Boltzmann, but 99.5% of the differences can be captured by a small correction which depends only on

the filling fraction. The isobaric granular NESS shows the standard signatures of a first-order phase transition including rate-dependent hysteresis. The main difference is that mechanical equilibrium still requires both phases to have equal pressures, which is guaranteed by the isobaric boundary condition, but the lack of energy conservation removes the ordinary requirement of thermal equilibrium, that both phases have the same temperature. Thus there exists a strong analogy between uniform granular NESS and ordinary equilibrium thermodynamics. In the future, we will test the analogy between local thermodynamic equilibrium and local uniform NESS in systems with gradients.

ACKNOWLEDGMENTS

We thank Ivo Nezbeda for allowing us to reproduce their numerical data presented in [4]. This work is funded by The National Science Foundation, Math, Physical Sciences Department of Materials Research under the Faculty Early Career Development (CAREER) Program (DMR-0134837). PMR was partially funded by the Portuguese Ministry of Science and Technology under the POCTI program and the MECHPLANT NEST-Adventure program of the European Union.

REFERENCES

1. P. M. Reis, R. A. Ingale, and M. D. Shattuck, *Phys. Rev. Lett.* **96**, 258001 (2006).
2. P. M. Reis, R. A. Ingale, and M. D. Shattuck, *Physical Review Letters* **98**, 188301 (2007).
3. P. M. Reis, R. A. Ingale, and M. D. Shattuck, *Physical Review E* **75**, 051311 (2007).
4. F. Moucka, and I. Nezbeda, *Phys. Rev. Lett.* **94**, 040601 (2006).
5. E.R. Weeks, J.C. Crocker, A.C. Levitt, A. Schofield and D.A. Weitz, *Science* **287**, 627 (2000).
6. H. König, R. Hund, Z. Zahn and G. Maret *Eur. Phys. J. E* **18**, 287 (2005).
7. M. M. Hurley and P. Harrowell *Phys. Rev. E* **52**, 1694 (1995). R. Zangi and S.A. Rice *Phys. Rev. Lett.* **92**, 035502 (2004).
8. A. Jaster, *Phys. Lett. A* **330**, 120 (2004).
9. J. S. Olafsen, and J. S. Urbach, *Phys. Rev. E* **60**, R2468–R2471 (1999). A. Prevost, D. A. Egolf, and J. S. Urbach, *Phys. Rev. Lett.* **89**, 084301 (2002).
10. W. Losert, D. G. W. Cooper, J. Delour, A. Kudrolli, and J. P. Gollub, *Chaos* **9**, 682 (1999). F. Rouyer, and N. Menon, *Phys. Rev. Lett.* **85**, 3676 (2000). D. L. Blair, and A. Kudrolli, *Phys. Rev. E* **64**, 050301(R) (2001). I. S. Aranson, and J. S. Olafsen, *Phys. Rev. E* **66**, 061302 (2002). D. L. Blair, and A. Kudrolli, *Phys. Rev. E* **67**, 041301 (2003).
11. A. Gotzendorfer, C. H. Tai, C. A. Kruelle, I. Rehberg, and S. S. Hsiau, *Physical Review E (Statistical, Nonlinear, and Soft Matter Physics)* **74**, 011304/1–9 (2006).
12. B. Bernal, *Proc. Roy. Soc. A* **280**, 299 (1964). P. M. Chaikin, *Principles of Condensed Matter Physics* (Cambridge University Press, U.K., 1995).
13. D. R. Nelson and B. I. Halperin, *Phys. Rev. B* **19**, 2457 (1979). A. Jaster, *Phys. Rev. E* **59**, 2594 (1999).
14. D. P. Fraser, M. J. Zuckermann and O. G. Mouritsen, *Phys. Rev. A* **42**, 3186 (1990).
15. P.N. Pusey and W. van Megen *Physica A* **157**, 705 (1989). W. van Megen and S.M. Underwood *Phys. Rev. E* **47**, 248 (1993).
16. H. Sillescu, *J. Non-Crystal. Solids* **243** 81 (1999). M. D. Ediger, *Annu. Rev. Phys. Chem.* **51**, 99 (2000).
17. W. Götz, in *Liquids, Freezing and Glass Transition*, edited by J. P. Hansen, D. Levesque, and J. Zinn-Justin (North Holland, Amsterdam, 1991). Les Houches Summer Schools of Theoretical Physics Session LI 287 (1989).
18. L. F. Cugliandolo, in *Slow Relaxations and nonequilibrium dynamics in condensed matter*, edited by J.-L. Barrat, M. Feigelman, J. Kurchan and J. Dalibard (Springer Berlin/Heidelberg) Les Houches Summer School, **77** 367 (2004).
19. J.-L. Barrat, J.-N. Roux and J.-P. Hansen *Chem. Phys.* **149**, 197 (1990).
20. O. Poulliquen, M. Belzons and M. Nicolas, *Phys. Rev. Lett.* **91**, 014301 (2003).
21. G. Marty and O. Dauchot, *Phys. Rev. Lett.* **94**, 015701 (2005). O. Dauchot, G. Marty and G. Biroli, *Phys. Rev. Lett.* **95**, 265701 (2006).
22. A.R. Abate and D.J. Durian, *Phys. Rev. E*, **74**, 031308 (2006).
23. S. J. Moon, M. D. Shattuck, and J. B. Swift, *Phys. Rev. E* **64**, 031303 (2001).
24. T. van Noije, and M. Ernst, *Granular Matter* **1**, 57–64 (1998).
25. D. L. Blair, and A. Kudrolli, *Phys. Rev. E* **67**, 041301 (2003).
26. S. Savage, and D. Jeffery, *J. Fluid Mech* **110**, 255 (1981). J. Jenkins, and M. Richman, *Arch. Ration. Mech. Anal.* **87**, 355 (1985). C. K. K. Lun, *J. Fluid Mech.* **233**, 539–559 (1991). A. Goldshtein, and M. Shapiro, *J. Fluid Mech.* **282**, 75–114 (1995). N. Sela, I. Goldhirsch, and S. H. Noskowitz, *Phys. Fluids* **8**, 2337–2353 (1996). T. P. C. van Noije, M. H. Ernst, and R. Brito, *Physica A* **251**, 266 (1998). V. Kumaran, *Physical Review Letters* **95**, 108001 (2005). J. J. Brey, and J. W. Dufty, *Physical Review E* **72**, 011303 (2005). J. F. Lutsko, *Physical Review E* **73**, 021302 (2006).
27. T. van Noije, and M. Ernst, *Granular Matter* **1**, 57–64 (1998). T. P. C. van Noije, M. H. Ernst, E. Trizac, and I. Pagonabarraga, *Phys. Rev. E* **59**, 4326–4341 (1999). J. Montanero, and A. Santos, *Granular Matter* **2**, 53–64 (2000). N. V. Brilliantov, and T. Poschel, *Europhys. Lett.* **74**, 424 (2006). T. Pöschel, N. V. Brilliantov, and A. Formella, *Phys. Rev. E* **74**, 041302 (2006).
28. J. Montanero, and A. Santos, *Granular Matter* **2**, 53–64 (2000).
29. T. Pöschel, N. V. Brilliantov, and A. Formella, *Phys. Rev. E* **74**, 041302 (2006).